CHEMISTRY
A EUROPEAN JOURNAL

FULL PAPER

DOI: 10.1002/chem.201203009

VIP

Structure-Dependent Electrocatalysis of $Ni(OH)_2$ Hourglass-like Nanostructures Towards L-Histidine

Jianwei Nai, Zhengbo Chen, Haopeng Li, Fangyuan Li, Yang Bai, Lidong Li,* and Lin Guo*[a]

Abstract: As the properties of nanomaterials are strongly dependent on their size, shape and nanostructures, probing the relations between macro-properties and nanostructures is challenging for nanoscientists. Herein, we deliberately chose three types of $Ni(OH)_2$ with hexagonal, truncated trigonal, and trigonal hourglass-like nanostructures, respectively, as the electrode modifier to demonstrate the correlation between the nanostructures and their electrocatalytic performance towards L-histidine. It was found that the hexagonal hourglass-like $Ni(OH)_2$ sample had the best electrocatalytic activity, which can be understood by a cooperative mechanism: on one hand, the hexagonal sample possesses the largest specific surface area and the tidiest nanostructure, resulting in the most orderly packing on the electrode surface; on the other hand, its internal structure with the most stacking faults would generate a lot of unstable protons, leading to an enhanced electronic conductivity. The findings are important because they provide a clue for materials design and engineering to meet a specific requirement for electrocatalysis of L-histidine, possibly even for other biomolecules. In addition, the hexagonal $Ni(OH)_2$-based biosensor shows excellent sensitivity and selectivity in the determination of L-histidine and offers a promising feature for the analytical application in real biological samples.

Keywords: biosensors · electrocatalysis · L-histidine · nanostructures · nickel

Introduction

New properties can be acquired from the materials at the nanoscale and, equally important, these properties change with their structure.[1] Therefore, a good understanding of the correlation between the structure and the property is regarded as a grand challenge that must be met for the researchers to improve the engineering of a desired nanostructure with specific properties. Nanomaterials with electrocatalytic activity have raised much attention since the early 2000s due to its wide application in carbon monoxide oxidation, alcohols oxidation, amino oxidation and other reactions of significant importance in environmental engineering as well as energy storage.[2] As we know, the electrocatalytic activity and sensitivity is highly structure-dependent.[3,4] So far, some researchers have systematically shown the importance of the tailoring of the structure under strictly controlled experimental conditions, and reported the dependence of the nanostructure on both electrochemical reactivity and selectivity.[5–14] Basically, the structure-dependent feature in electrocatalysis can be roughly divided into three categories: size-,[5,6] shape-[7,8] and composition dependence.[9–14] The size effect is common for nanoscale materials with a high specific surface area. Recently, the group of Zheng[15] reported the synthesis of ultra-thin Pd nanosheets restricted to less than 10 atomic layers, which exhibited 2.5 times as electrocatalytic active as that measured for high-surface-area commercial Pd for the oxidation of formic acid. Shape-controlled electrocatalytic sensitivity is generally considered because nanomaterials with well-defined facets can show specific activity or selectivity compared with those materials exposed with common planes. By using a programmed electrochemical method, Tian et al.[16] prepared single-crystallite tetrahexahedral Pt nanocrystals and found that the high index planes, such as {730}, {210} or {520}, exhibited greatly enhanced (up to 400%) catalytic activity compared with equivalent Pt surface areas for the electrooxidation of formic acid and ethanol. This remarkable catalytic performance at the high index planes could also be demonstrated by Liu and co-workers.[17] They investigated the ethanol oxidation on different Pt crystal planes by density functional theory calculations and showed that the selectivity of ethanol oxidation depended markedly on the surface structure. When it comes to the composition-dependent electrocatalytic activity, a synergistic effect of the components should be responsible for the activity improvement. Fang et al.[18–20] studied the electrochemical properties of PtCu nanoparticles and found that for methanol oxidation, the catalytic activity followed the order: PtCu nanocube > PtCu nanosphere > Pt

[a] Dr. J. Nai,[+] Z. Chen,[+] H. Li, F. Li, Y. Bai, Prof. L. Li, L. Guo
School of Chemistry and Environment
Beihang University
Beijing, 100191 (P.R. China)
E-mail: lilidong@buaa.edu.cn
guolin@buaa.edu.cn

[+] These authors contributed equally to this work.

Supporting information for this article is available on the WWW under http://dx.doi.org/10.1002/chem.201203009.

nanosphere. It is also shown that cubic PtCu nanoparticles were more active than spherical PtCu nanoparticles for the formic acid oxidation at high potentials. According to the above literature, most of the efforts were made to explore the relation between the nanostructures and their electrocatalytic properties in the fields of poisonous gas treatment and fuel cells, but few[8] in biosensing, particular in the detection of amino acids.

L-Histidine, a neurotransmitter or neuromodulator, is an essential bioactive amino acid which plays a significant role in physiologic antioxidant defenses. It has long been known as a fairly efficient scavenger of both the hydroxy radical[21] and the nonradical toxic oxygen species singlet oxygen,[22] which is emerging as an important contributing factor in many deleterious oxidative processes. As a result, histidine-containing medicaments have the potential to be anti-inflammatory therapeutic agents in a range of diseases, including ulcerative colitis, infectious diarrhea, bacterial meningitis, cardiac ischemia, and respiratory distress syndrome.[23] However, ingesting very large doses of L-histidine would induce minor neurologic symptoms, such as taste and smell distortion.[24] Therefore, sensitive detection of L-histidine is very important from the perspective of applications in both drug research and clinical treatment. Besides, investigating the correlation between the nanostructures and their electrocatalytic performance is undoubtedly vital and helpful for the researchers to select a proper nanostructure for the highly sensitive detection of L-histidine.

As we know, $Ni(OH)_2$ possesses high catalytic activity towards electrooxidation of organics containing OH or NH_2 groups.[25] In addition, it has a wide application in sensors for ethanol,[26] urea,[27] glucose,[28] drugs,[29,30] amino acids,[31,32] and DNA[33] through cyclic-mediated electron-transfer processes in alkaline solutions. Moreover, compared with pure Ni or NiO, a $Ni(OH)_2$-modified electrode with more direct, stable,[28] low-cost, and low-toxic[34] features should be more suitable and promising for the eco-friendly and high-efficiency biochemical detection nowadays. In this paper, the morphology and growth mechanism of three types of hourglass-like $Ni(OH)_2$ nanomaterials including hexagonal, truncated trigonal, and trigonal,[35] are briefly represented at first for helping to understand their external and internal structures. Then these unique nanostructures were chosen as the electrode modifier separately to detect the L-histidine. Based on the experimental results, we discuss in detail the correlation between the nanostructures and their electrocatalytic performance on L-histidine. In addition, the hexagonal hourglass-like $Ni(OH)_2$, which shows the best electrocatalytic properties toward L-histidine, was also selected for testing its analytical application in real biological samples.

Results and Discussion

Morphology characterization and growth mechanism of three types of hourglass-like $Ni(OH)_2$: Figure 1a illustrates the crystallographic structural characteristics of the three types of hourglass-like $Ni(OH)_2$ nanomaterials investigated by using XRD analysis. All of the diffraction peaks of each sample can be indexed as β-phase nickel hydroxide (JCPDS 14-0117). The relative peak intensity of 101/001 increases obviously from the hexagonal to the trigonal sample, indicating a different evolution of pyramidal planes of the crystals, $R\{101\}$ and $r\{-101\}$, among the three types of nanostructure.

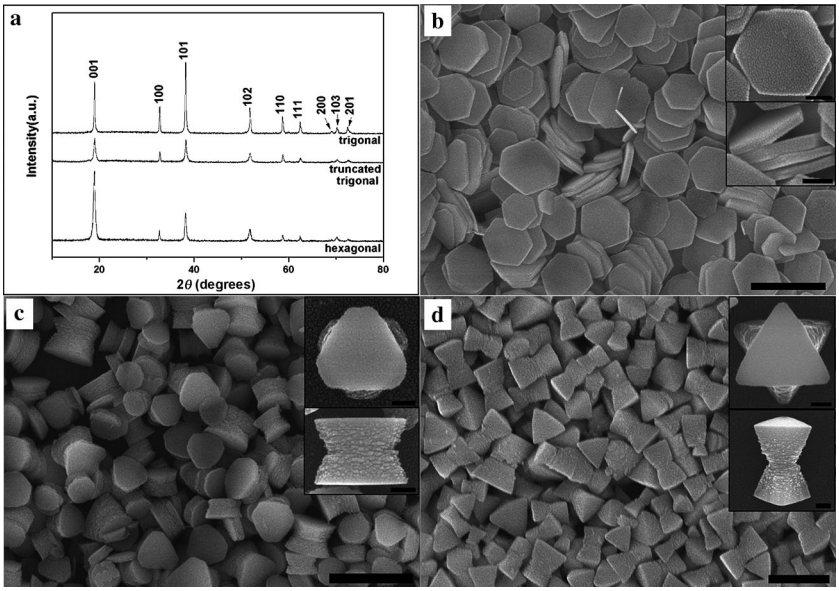

Figure 1. a) XRD patterns of three types of hourglass-like $Ni(OH)_2$ nanocrytstals. The relative peak intensity of 101/001 clearly increases from the hexagonal to the trigonal sample, indicating a different evolution of pyramidal planes of the crystals among the three types of nanostructures. SEM overview images of b) hexagonal, c) truncated trigonal, and d) trigonal hourglass-like $Ni(OH)_2$ nanomaterials. Insets of each image are the top view and side view of the corresponding nanostructure. The scale bars of the SEM overview images and insets are 500 and 100 nm, respectively.

Typical SEM images of the samples are shown in Figure 1b–1d. Figure 1b shows the sample with stunted hexagonal hourglass-like architecture that is similar to the "nanoplate" morphology. As shown in the inset of Figure 1b, the average side length and height of the hexagonal hourglass-

like sample are about 180 nm and 50 nm, respectively. Figure 1c shows the morphology of the truncated trigonal sample, in which an obvious concave polyhedron with centrosymmetric hourglass-like structure is obtained. A particular crystal is evident with 280/120 nm in average long/short side length of the top (bottom) truncated triangle, and with 270 nm in height. The magnified images shown in the insets provide clear top and side views of the mesosoma hourglass structure. A well-developed hourglass nanocrystal, which is elongated compared with the two previous samples, is also obtained and shown in Figure 1d. The average side length of the top (bottom) triangle is 400 nm and the height prolongs to be about 500 nm. Obviously, each β-$Ni(OH)_2$ concave polyhedron could be seen as two truncated pyramids joining together with a central-symmetry manner. The pyramidal faces (side faces) can be classified into two shapes, isosceles triangles and trapezoids, which are presented alternately along the pyramidal side.

From our previous work,[35] it has been proven that the amount of hydrazine hydrate determines the evolution of the crystallographic pyramidal planes of the crystals, $R\{101\}$ and $r\{-101\}$, which should answer for the enlarging area of the pyramidal faces. Besides, a growth mechanism based on two-stage oriented attachment has also been proposed and perfectly explained the series of anisotropic features as well as the interesting structural pattern of the as-prepared β-$Ni(OH)_2$ hourglass-like nanofamily. Basically, the $Ni(OH)_6^{4-}$ coordination octahedron (NCO) is considered to serve as the basic growth unit to fabricate these nanocarystals. It can be observed from Figure 2a that the NCOs in one layer are exposing their faces at $R\{101\}$ planes, whereas exposing their corners at $r\{-101\}$ planes. In general, with this spatial relationship between the octahedra and the pyramidal planes families, the stacking of the NCOs along the $r<-101>$ direction should be more stable and then grow faster than the $R<101>$ direction. As shown in Figure 2b, when the amount of $N_2H_4{\cdot}H_2O$ is low (0.5 mL), the evolution of R and r planes in the hexagonal crystal is poor, thus the two types of pyramidal faces (A and B) would be both restrained to growth and show nearly no difference in their areas ($A/B \approx 1$), favoring the hexagonal shape of the top (bottom) faces. When we increased the amount of $N_2H_4{\cdot}H_2O$, the height of the nanocrystal increased. The pyramidal faces B that correspond to the evolution of r planes would gradually reduce; whereas the alternate faces A that correspond to the evolution of R planes would expand, leading to the formation of an intermediate morphology, which is the truncated-trigonal nanostructure. If we kept increasing the amount of $N_2H_4{\cdot}H_2O$ to some extent (3.0 mL), pyramidal faces A would keep enlarging at the cost of reduction of the alternate faces B. As a result, the trigonal hourglass-like nanostructures will form because of the area ratio of A/B increases to its maximum value. And the top (bottom) faces would thus show equilateral triangles. Of note, herein, the hexagonal morphology termed as the stunted "hourglass-like" nanostructures would be more appropriate than the "plate-like" nanostructures in this crystal family.

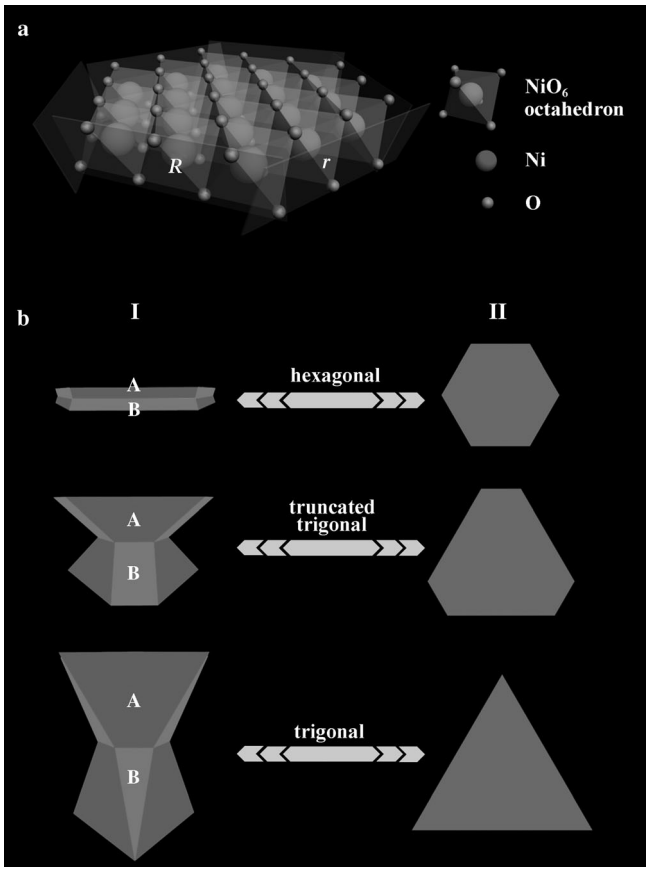

Figure 2. a) The spatial relationship between the stacking NCOs and the R or r planes (the hydrogen atoms are omitted for clarity); the stacking of the NCOs along the r direction should be more stable and grow faster than the R direction. b) The shape evolution of the pyramidal faces (column I) and corresponding top (bottom) face (column II) from the hexagonal to the trigonal nanostructure; pyramidal faces A and B correspond to the evolution of R and r planes, respectively. From the hexagonal to trigonal, with increasing height of the nanocrystal, the pyramidal faces A gradually expand at the cost of reduction of the alternate faces B. A color version is available in the Supporting Information as Figure S14.

Electrocatalytical performance of the hourglass-like $Ni(OH)_2$ nanostructures: Basically, the electrocatalytic oxidation mechanism of L-histidine on the $Ni(OH)_2$ nanocrystal-modified electrode can be explained by the following equations:

$$Ni(OH)_2 + OH^- \rightleftharpoons NiOOH + H_2O + e^- \quad (1)$$

$$NiOOH + \text{L-histidine} \rightarrow \text{product} + Ni(OH)_2 \quad (2)$$

A detailed electrocatalytic mechanism is illustrated in Scheme 1. Firstly, $Ni(OH)_2$ was oxidized at the electrode surface to NiOOH. Then adsorbed L-histidine reduced NiOOH back to $Ni(OH)_2$, which would be electrochemically reoxidized in the CV procedure. Meanwhile, the oxidation of L-histidine was possible after the NiOOH was electrochemically formed, in which the N-end segment of the L-histidine molecule ($-CH_2-NH_2$) might be converted into nitrile ($-CN$).[31,32,36] In addition, decarboxylation can occur[37] in

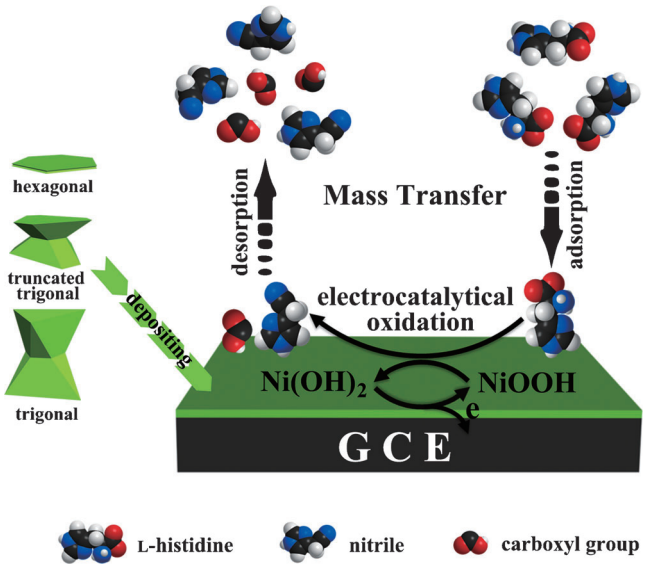

Scheme 1. Schematic illustration of the electrocatalytic oxidation mechanism of L-histidine on the $Ni(OH)_2$ nanocrystal-modified GCE. The atoms in organic groups: black, C; white, H; red, O; blue, N.

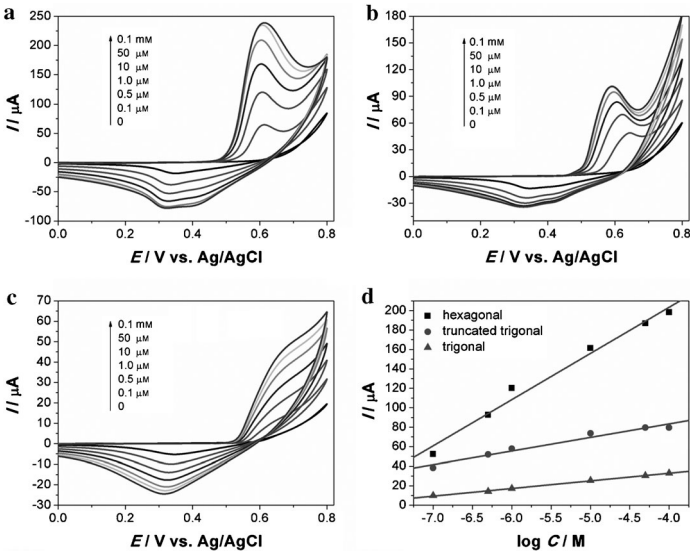

Figure 3. CVs obtained at GCE modified with the 0.625 $g L^{-1}$ a) hexagonal, b) truncated trigonal, and c) trigonal hourglass-like $Ni(OH)_2$ in a solution of NaOH (0.1 M) with various concentrations of L-histidine at the scan rate of 0.05 $V s^{-1}$. The peak currents increase with the increasing concentration of L-histidine. d) The oxidation peak currents of the CVs in a, b, and c as a function of specific L-histidine concentrations. The hexagonal sample shows the best electrocatalytical performance among the three hourglass-like samples for the detection of L-histidine.

the presence of an α-amino group and thus generate carboxyl group, which is a common one-carbon unit degraded from histidine.[38,39]

By depositing different types of $Ni(OH)_2$ nanomaterials with the same concentration (0.625 $g L^{-1}$) on the surface of the glassy carbon electrode (GCE), three simple biosensors were prepared. Then, the sensing performance of $Ni(OH)_2$ modified electrodes for L-histidine were evaluated through cyclic voltammetry (CV) measurement in a solution of NaOH (0.1 M). Typical CV curves obtained at the $Ni(OH)_2$/GCE when reacting with various concentrations of L-histidine ranging from 0.1 μM to 0.1 mM are shown in Figure 3 a, b, and c. Some similar features of the CVs can be summarized as follows: 1) Prior to interaction with L-histidine, no obvious oxidation peak current can be detected. 2) When adding very small amount of L-histidine (0.1 μM), the oxidation peak currents dramatically enhance. With increasing the concentration of L-histidine, it is observed that the oxidation peak currents gradually increase, indicating that L-histidine is oxidized. 3) It should be noted that, this electrochemical behavior is different from typical mediated catalytic oxidation in which the reduction peak current is expected to decrease. An increase in the oxidation- and reduction peak currents after L-histidine addition is believed to be due to the fact that the transition between $Ni(OH)_2$ and NiOOH makes this redox couple have a dual function as the electronic medium and catalyst, synchronously.[40] 4) In the present of L-histidine, the potentials of oxidation peak slightly shift but are all close to that of the intrinsic $Ni(OH)_2$/NiOOH transition, also suggesting the existence of electron transfer between the histidine and the $Ni(OH)_2$/NiOOH couple. 5) CVs obtained from various scan rates show that the kinetic process is diffusion-controlled in each electrochemical system of the three samples (Figure S1 in the Supporting Information). Meanwhile, differences also apparently exist. 1) The oxidation peak current of the electrode with the $Ni(OH)_2$ modifier follows the sequence of hexagonal > truncated trigonal > trigonal, as shown in Figure 2 d. The hexagonal sample shows the best electrocatalytical performance among the three hourglass-like samples for the detection of L-histidine. This superiority becomes more and more obvious as the concentration of L-histidine increases, and at an L-histidine concentration of 0.1 mM, the oxidation peak current of the electrode with hexagonal modification is about 3- and 9-fold higher than that with truncated trigonal $Ni(OH)_2$ and trigonal $Ni(OH)_2$ modification, respectively. In addition, the detection limit of the electrode modified with the hexagonal sample is 12.9 nM as calculated in terms of the 3σ rule,[41] which is the lowest among three samples; whereas the detection limit of the electrode modified with truncated trigonal sample and trigonal sample are 41.4 nM and 66.8 nM, respectively. 2) Only one reduction peak located at 0.32 V can be observed in the CVs of trigonal sample, whereas another small peak around 0.42 V is detected in the CVs of truncated trigonal sample, and this peak is more obvious in that of the hexagonal sample. The reason of this phenomenon might be that compared with other two samples, the hexagonal sample has the best electrocatalytical ability, and then the most amount of product would be generated after the oxidation of L-histidine, which would probably desorb from the surface of electrode and induce a current response at the peak of 0.42 V. The fact that this specific peak becomes more obvious as the concentration of L-his-

tidine increases (as shown in Figure 3a) also supports the inference above.

As the electrochemical performance of the electrode can be influenced by the amount of the as-deposited materials, we increased the concentration of the three types of $Ni(OH)_2$ samples to 2.5 and 5.0 $g\,L^{-1}$, respectively, for further electrocatalytic experiments. CVs obtained from the electrode modified with 2.5 and 5.0 $g\,L^{-1}$ $Ni(OH)_2$ samples (the Supporting Information, Figures S2 and S3) demonstrated similar results as that with 0.625 $g\,L^{-1}$ (Figure 3): the electrocatalytical activity follows the sequence of hexagonal > truncated trigonal > trigonal. If one considers the distinct size difference of three types of $Ni(OH)_2$ crystal particles, then another reasonable comparison of their electrocatalytical performance should guarantee that the amount of the three types of crystal particles deposited on the electrode surface is either the same or that the difference is negligible. Herein, if the $Ni(OH)_2$ molecular packing densities in a crystal particle of three types of morphologies are supposedly the same, then the mass ratio of a crystal particle should be: hexagonal/truncated trigonal/trigonal $\approx$ 1:4:8, in terms of their volume ratio. Hence, the comparison of the electrocatalytical activity among the hexagonal with 0.625 $g\,L^{-1}$, truncated trigonal with 2.5 $g\,L^{-1}$ and trigonal with 5.0 $g\,L^{-1}$ can meet the request above (0.625:2.5:5.0 = 1:4:8). Interestingly, this comparison still shows that the hexagonal sample has the best electrocatalytical activity (the Supporting Information, Figure S4). All the experimental data reveal that the intrinsic properties of this crystal family present fascinating electrocatalytic results.

Understanding of the structure-dependent electrocatalytic performance: Herein, we believe two important factors, the external architecture and the internal degree of crystallinity, should be mainly put into consideration.

Consideration of the external architecture: As shown in Figure 2b, three samples all belong to the hourglass-like nanocrystal family, with six pyramidal faces, one top face and one bottom face. They differ only in the crystal height, shape, and areas of each faces. Although the trigonal structure could adsorb more histidine molecules than the hexagonal structure concerned with a crystal particle (the Supporting Information, Figure S5), the smaller hexagonal sample with a higher specific surface area still has the chance to adsorb more histidine molecules than the trigonal sample under the same concentration of the modified material. Additionally, the hexagonal sample possess inherent structural superiority of two-dimensional (2D) nanostructure, that is, stacking more compactly among the crystal particles and being much easier to form a relatively ordered configuration,[42] than the trigonal sample with three-dimensional (3D) sophisticated architecture when depositing on GCE. Moreover, the trigonal sample featured with the largest particle size has the difficulty in achieving complete oxidation during the charge process, which might also be responsible for its relatively worse electrocatalytic activity.

Consideration of the internal degree of crystallinity: It has been reported that some structural defects or disorders could be incorporated during the crystallization of nickel hydroxide, resulting in poor crystallinity but better electrochemical performance.[43–47] Basically, these disorders can be divided into: a) cation vacancies,[48,49] b) stacking faults,[43,44] c) turbostratic disorders[50] involving the random orientation of the layers about the *c*-crystallographic axis, and d) interstratification[51] arising due to the insertion of water molecules and/or anions part of the way between the hydroxide layers. Based on the literature, the cation (Ni^{2+}) vacancies and the interstratification would give rise to the lowering of point group symmetry as well as the obvious change of crystallographic structural parameter;[46] whereas the turbostratic disorder would lead to the *hk*0 (e.g., 100 and 110) reflections acquire a "saw tooth" line shape, displaying an asymmetry on the higher-angle side.[52] However, no such proof can be obtained from the XRD patterns in our work (Figure 1a), suggesting that almost none of these three kinds of disorders could be involved in the crystal formation of the as-prepared $Ni(OH)_2$ nanofamily. Stacking faults, nevertheless, which can strongly affect the full width at half-maximum (FWHM) value of *h*0*l* reflections,[43] were revealed in our XRD patterns (the Supporting Information, Figure S6). The patterns demonstrate that the FWHM values of 101 and 102 peaks of the hexagonal sample are obviously larger than those of the other two samples, indicating the existence of a greater amount of stacking faults in the hexagonal sample. Thus, the correlation between the nature of stacking faults and electrocatalytic performance of nickel hydroxide needs to be further illustrated.

By employing symbols A, B, and C to represent hydroxyl group positions, a typical ideal crystallographic structure of nickel hydroxide is supposed to have the stacking sequence of ABAB (Figure 4a), which represents the single-layered periodicity of a hexagonal lattice.[53] Stacking faults are introduced by the insertion of the other types of hydroxide layers, such as BA, CA, CB and so on, amidst the primary

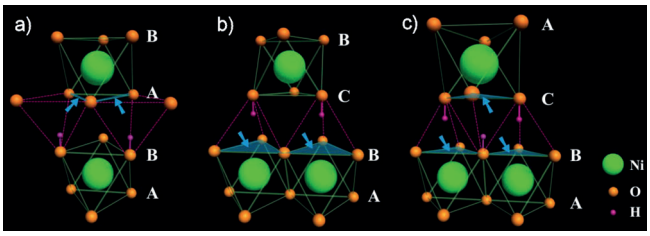

Figure 4. Polyhedra linkages illustrating the stacking manner of nickel hydroxide: a) in the ideal structure (ABAB oxygen stacking), in which the HO_4 tetrahedron and the NiO_6 octahedron share only one edge (highlighted by arrows), therefore, H is relatively stable; b) on a growth stacking fault (ABCB oxygen stacking) and c) on a deformation stacking fault (ABCA oxygen stacking), in which the HO_4 tetrahedron and the NiO_6 octahedron share one face (highlighted by arrows), therefore, H is unstable. Note: here, the HO_4 tetrahedra are delineated by pink dotted lines. The illustration indicates that the more stacking faults embedded, the more unstable protons are generated, leading to an enhanced electrocatalytic activity..

ABAB stacking manner. From a general point of view,[43,44] the insertion of CB and CA layers were considered as the main types of stacking faults in nickel hydroxide, named as "growth faults" and "deformation faults", respectively. Layer CA is related to AB by a (1/3, 2/3, 1) translation, whereas CB by a combination of (1/3, −1/3, 1) translation and a mirror-plane (001) reflection. Insertion of these various layers into the primary sequence generates different interlayer sites. As shown in Figure 4b, the insertion of a CB layer leads to the generation of only octahedral interlayer sites, whereas the CA layer (Figure 4c) generates an octahedral and a trigonal prismatic interlayer site. Figure 4 also shows the relative space relations between the hydrogen atom of a hydroxide slab and the nickel ion of the next slab, among these three types of stacking manners. The nickel atom is always located in the center of the NiO_6 octahedra. The hydrogen atoms, in the interslab space, are exactly above or under the oxygen atoms by O−H bonding. Thus, H atom can be considered as in the center of HO_4 tetrahedra. In an ideal structure (Figure 4a), the electrostatic interaction between a hydrogen atom and a nickel ion is quite small because they are relatively far away from each other (the HO_4 tetrahedron and the NiO_6 octahedron share only one edge, delineated by an arrow). However, in the vicinity of a stacking fault (Figure 4b and 4c), this interaction is much stronger as these two polyhedra share one face (delineated by arrow), which is in violation of the third Pauling rule, therefore this means the hydrogen atoms localized at the stacking faults are unstable with respect to the others. Actually, Equation (1) can be spatially separated into $OH^- + H^+ \rightarrow H_2O$ at the electrode/electrolyte interface and $Ni(OH)_2 \rightarrow NiOOH + H^+ + e^-$ within the solid phases. A diffusion step is therefore necessary to move protons from the site in which they are created to the charge-transfer site, through the solid material. Thus, during the oxidation of $Ni(OH)_2$, these unstable hydrogen atoms can be more easily deintercalated. One can assume that during the following reduction process, the protons will not be easily reintercalated into these sites. This means that the more stacking faults involved, the more unstable protons are generated, leading to the persistence of more trivalent nickel ions, which may provide an enhanced local electrical conductivity. Thus, more protons could participate in the electron-transfer at the heterogeneous catalytic interface and improve the electrocatalytic activity. Meanwhile, the presence of these hydrogen atoms in a different surrounding might explain the appearance of new lines in the Raman spectra (the Supporting Information, Figure S7). The specific peak located at 510 cm^{-1} in the spectrum of the hexagonal sample (the Supporting Information, Figure S7d), should be associated with the existence of proton vacancies.[54] Hence, the stacking faults could be caused by these proton vacancies induced by the existence of H_2O molecules in β-$Ni(OH)_2$, which has been demonstrated.[55] From this viewpoint, the reason the current signal of CVs of the hexagonal $Ni(OH)_2$ sample is the highest could be also easily understood because the proton vacancies would enhance the proton diffusion coefficient of the sample. This defect- or disorder-induced enhancement of catalytic activity has also recently been found in some other metal oxide nanomaterials.[56–58]

Furthermore, we further experimented by synthesizing $Ni(OH)_2$ nanostructures with thinner thickness compared with the 50 nm hexagonal sample. The characterization results (the Supporting Information, Figure S8) demonstrate that 101 and 102 peaks in XRD of the as-prepared nanocrystal are wider than previous samples, indicating greater amounts of the embedded stacking faults. The morphology is also hexagonal, but its thickness along the *c* axis of $Ni(OH)_2$ is only about 20 nm. Cyclic voltammetry was operated on the electrode modified with the concentration of 0.625 $g\,L^{-1}$ of this sample. The results show that the 20 nm-hexagonal sample is better than all the previous samples in detecting of L-histidine under the same concentration (the Supporting Information, Figure S9). When guaranteeing that the number of the crystal particles is the same, the CVs obtained with 0.25 $g\,L^{-1}$ 20 nm-hexagonal sample should be a reasonable result for comparison since 0.25:0.625 = 2:5, which is approximately the mass ratio of the two hexagonal samples. Fascinatingly, the result still reveals this 20 nm-hexagonal sample has the best electrocatalytic activity among the four samples under the same particle numbers (the Supporting Information, Figure S10). These data again prove our argument that the simpler the morphology and the more embedded stacking faults, the better electrocatalytic activity of the sample for L-histidine.

In addition, from a thermodynamic point of view, the introduction of stacking faults would apparently change neither the coordination number nor the octahedral symmetry about the Ni^{2+} ion. Therefore, stacking faults do not diminish the enthalpy of the system, but by increasing the disorder contribute towards a marginal lowering of the free energy through the entropy term. Concomitant with the higher thermodynamic stability of the stack faulted phases, the point group symmetry around the Ni^{2+} ion would increase from $\bar{3}m$ to 6/*mmm*.[46] Herein, although the XRD patterns of the three samples are very similar with the standard pattern of nickel hydroxide (point group: $P\bar{3}m1$, as shown in the Supporting Information, Figure S11), the pattern of hexagonal sample with relative lower peak intensity and broader FWHM of 101 or 102 should be attributed to a different symmetry, which is likely to be 6/*mmm*. In this work, the morphology of the samples transfers from trigonal to hexagonal hourglass-like nanostructures with the increasing symmetry from $\bar{3}m$ to 6/*mmm*, which is in accordance with the general viewpoint that the macroscopic morphology of the crystal is usually bound up with its microscopic symmetry of the crystallographic structure. Verma and Krishna[59] have argued that polytypes having a higher symmetry have greater thermodynamic stability. Extending this argument to faulted crystals in our work, hexagonal crystals having more stacking faults are expected to have a higher thermodynamic stability than the other two kinds of nanocrystals, which should be theoretically in favor of practical testing.

Application to real samples by using a 50 nm-hexagonal $Ni(OH)_2$-modified electrode: Although all three types of hourglass-like $Ni(OH)_2$ samples show much better electrocatalytic sensitivity than the commercial sample (the Supporting Information, Figure S12), the hexagonal sample with the best electrocatalytic performance is considered as most suitable for real sample test based on the discussion above. The liner range of this sample (0.1 μM–0.1 mM) perfectly covers the normal concentration value (ca. 10 μM) of L-histidine in human body, indicating that it is good enough for analysis of real samples. Besides, the detection limit for L-histidine was 12.9 nM, which is significantly lower than those previously reported.[60–62] Hence, we tested a human blood serum sample with different L-histidine concentrations on the hexagonal $Ni(OH)_2$-modified GCE. The analytical results reveal that the recovery and relative standard deviation values are acceptable (the Supporting Information, Table S1). In addition, the selectivity of this biosensor has also been studied by challenging it with other interferences, such as, D-histidine, glucose, and ascorbic acid (the Supporting Information, Figure S13). The results reveal that the oxidation peaks of L-histidine can be distinguishable from the interferences. All these experimental data imply that our proposed biosensor has a promising feature for analytical application in complex biological samples.

Conclusion

A series of hourglass-like $Ni(OH)_2$ nanostructures were deliberately selected to serve as electrode modifiers and we have demonstrated the correlation between the structure of nanomaterials and their electrocatalytic activity on L-histidine. It was found that all three types of $Ni(OH)_2$ nanostructure modified electrodes have lower detection limit and wider linear range than the commercial materials. Moreover, the electrocatalytical performance of the hexagonal $Ni(OH)_2$ sample is the best under different test criterion. This should attribute to its superior external geometric construction and the internal structural stacking faults. The electrocatalytical activity of a simpler morphology, hexagonal $Ni(OH)_2$ nanostructures with a thickness of 20 nm, also support the basic argument of this paper. The findings are important because they firstly provide a clue for materials engineering to meet a specific requirement in L-histidine detection, possibly even for other target sensing. It also provides another opportunity for designing new and better electrocatalytic materials by using shape-controlled nanoparticles. In addition, the hexagonal hourglass-like $Ni(OH)_2$-based biosensor shows excellent sensitivity and selectivity in the determination of L-histidine and can offer a promising feature for the analytical application in real biological samples.

Experimental Section

Reagents: Nickel(II) 2,4-pentanedionate ($Ni(acac)_2$, 95%) was purchased from Alfa-Aesar Reagent Company. Commercial nickel hydroxide was obtained from Aladdin Reagent Company. Cetyltrimethylammonium bromide (CTAB) and hydrazine monohydrate ($N_2H_4{\cdot}H_2O$, 80%) were both obtained from Tianjin Fine Chemical Co. Ltd. L-Histidine was purchased from CNS Bioservices. All chemicals were of analytical grade and used without further purification.

Synthesis of the three types of hourglass-like β-$Ni(OH)_2$ nanocrystals: In a typical procedure,[35] 0.051 g of $Ni(acac)_2$ and 0.779 g CTAB were first dissolved into deionized water (50 mL) at room temperature, yielding a light-green transparent solution. After 30 min of vigorous agitation, 0.5 mL, 1.5 mL, and 3.0 mL $N_2H_4{\cdot}H_2O$ were introduced dropwise into the mixture for the synthesis of hexagonal, truncated trigonal and trigonal hourglass-like samples, respectively, turning the color of solution slowly to light bluish-purple. With another 30 min of stirring, the solution was heat to 80 °C for 5 h. Finally, a green precipitate was obtained that was rinsed several times with ethanol and deionized water.

Synthesis of hexagonal β-$Ni(OH)_2$ nanocrystals (20 nm-thickness): The typical procedure is nearly the same as that of the synthesis of hourglass-like β-$Ni(OH)_2$ nanocrystals above except the amount of $N_2H_4{\cdot}H_2O$ added is 0.3 mL.

Sample characterization: The structures and compositions of the as-prepared products were characterized by X-ray powder diffraction (XRD) using a Rigaku Dmax2200 X-ray diffractometer with $Cu_{K\alpha}$ radiation ($\lambda =$ 1.5416 Å). The morphologies of the synthesized samples were studied by a Hitachi S4800 cold-field emission scanning electron microscope (CFESEM). Transmission electron microscopy (TEM) and high-resolution TEM (HRTEM) investigations were carried out by a JEOL JEM-2100F microscope. Raman spectra were collected using a Jobin Yvon (Laboratory RAM HR800) confocal micro-Raman spectrometer equipped with a multi-channel charge-coupled detector. The Ar^+ laser emitting at a wavelength of 514.5 nm was used as a source of excitation. The number of grating in the Raman spectrometer was 600. The spectra were obtained using a 50× objective lens.

Electrode modification and electrochemical measurements: Prior to the modification, the glassy carbon electrode (GCE) surface was carefully polished to a mirror-like surface with alumina powders (0.05 μm) and then sonicated successively in ethanol and deionized water for 5 min, separately. Secondly, a $Ni(OH)_2$/deionized water solution (5 μL) of certain concentration was droplet-deposited on the surface of GCE and dried in air for further use. The electrochemical measurements were carried out with electrochemical analyzer (CHI 660C, CH Instruments) in a conventional three-electrode cell. The as-prepared modified electrode was used as a working electrode. An Ag/AgCl (sat. KCl) and a Pt wire were employed as reference electrode and counter electrode, respectively.

Acknowledgements

This work was supported by the National Basic Research Program of China (No. 2010CB934700), the National Natural Science Foundation of China (No. 20903008, 20973019 and 50725208).

[1] C. Burda, X. Chen, R. Narayanan, M. A. El-Sayed, *Chem. Rev.* **2005**, *105*, 1025–1102.
[2] J. Solla-Gullón, F. J. Vidal-Iglesias, J. M. Feliu, *Annu. Rep. Prog. Chem. Sect. C* **2011**, *107*, 263–297.
[3] K. Zhou, Y. Li, *Angew. Chem.* **2012**, *124*, 622–635; *Angew. Chem. Int. Ed.* **2012**, *51*, 602–613.
[4] M. T. M. Koper, *Nanoscale* **2011**, *3*, 2054–2073.
[5] C. Koenigsmann, A. C. Santulli, E. Sutter, S. S. Wong, *ACS Nano* **2011**, *5*, 7471–7487.

[6] C. Koenigsmann, W. Zhou, R. R. Adzic, E. Sutter, S. S. Wong, *Nano Lett.* **2010**, *10*, 2806–2811.
[7] H. Zhang, J.-J. Xu, H.-Y. Chen, *J. Phys. Chem. C* **2008**, *112*, 13886–13892.
[8] J. Wang, J. Gong, Y. Xiong, J. Yang, Y. Gao, Y. Liu, X. Lu, Z. Tang, *Chem. Commun.* **2011**, *47*, 6894–6896.
[9] A.-X. Yin, X.-Q. Min, Y.-W. Zhang, C.-H. Yan, *J. Am. Chem. Soc.* **2011**, *133*, 3816–3819.
[10] C.-L. Lu, K. S. Prasad, H.-L. Wu, J. A. Ho, M. H. Huang, *J. Am. Chem. Soc.* **2010**, *132*, 14546–14553.
[11] Z. Chen, D. Cummins, B. N. Reinecke, E. Clark, M. K. Sunkara, T. F. Jaramillo, *Nano Lett.* **2011**, *11*, 4168–4175.
[12] H. Abe, F. Matsumoto, L. R. Alden, S. C. Warren, H. D. Abruña, F. J. DiSalvo, *J. Am. Chem. Soc.* **2008**, *130*, 5452–5458.
[13] Y. Kang, C. B. Murray, *J. Am. Chem. Soc.* **2010**, *132*, 7568–7569.
[14] Y. Li, Z. W. Wang, C.-Y. Chiu, L. Ruan, W. Yang, Y. Yang, R. E. Palmer, Y. Huang, *Nanoscale* **2012**, *4*, 845–851.
[15] X. Huang, S. Tang, X. Mu, Y. Dai, G. Chen, Z. Zhou, F. Ruan, Z. Yang, N. Zheng, *Nat. Nanotechnol.* **2011**, *6*, 28–32.
[16] N. Tian, Z.-Y. Zhou, S.-G. Sun, Y. Ding, Z. L. Wang, *Science* **2007**, *316*, 732–735.
[17] H.-F. Wang, Z.-P. Liu, *J. Am. Chem. Soc.* **2008**, *130*, 10996–11004.
[18] D. Xu, Z. Liu, H. Yang, Q. Liu, J. Zhang, J. Fang, S. Zou, K. Sun, *Angew. Chem.* **2009**, *121*, 4281–4285; *Angew. Chem. Int. Ed.* **2009**, *48*, 4217–4221.
[19] H. Yang, L. Dai, D. Xu, J. Fang, S. Zou, *Electrochim. Acta* **2010**, *55*, 8000–8004.
[20] D. Xu, S. Bliznakov, Z. Liu, Z. Fang, N. Dimitrov, *Angew. Chem.* **2010**, *122*, 1304–1307; *Angew. Chem. Int. Ed.* **2010**, *49*, 1282–1285.
[21] I. Zs. -Nagy, R. A. Floyd, *Biochim. Biophys. Acta Protein Struct. Mol. Enzymol.* **1984**, *790*, 238–250.
[22] I. B. C. Matheson, J. Lee, *Photochem. Photobiol.* **1979**, *29*, 879–881.
[23] A. M. Wade, H. N. Tucker, *J. Nutr. Biochem.* **1998**, *9*, 308–315.
[24] R. I. Henkin, B. M. Patten, P. K. Re, D. A. Bronzert, *Arch. Neurol.* **1975**, *32*, 745–751.
[25] A. Ciszewski, G. Milczarek, B. Lewandowska, K. Krutowski, *Electroanalysis* **2003**, *15*, 518–523.
[26] P. Cox, D. Pletcher, *J. Appl. Electrochem.* **1990**, *20*, 549–5553.
[27] M. Vidotti, M. Silva, R. Salvador, S. Torresi, L. Dallantonia, *Electrochim. Acta* **2008**, *53*, 4030–4034.
[28] A. Safavi, N. Maleki, E. Farjami, *Biosens. Bioelectron.* **2009**, *24*, 1655–1660.
[29] S. Majdi, A. Jabbari, H. Heli, *J. Solid State Electrochem.* **2007**, *11*, 601–607.
[30] M. Hajjizadeh, A. Jabbari, H. Heli, A. Moosavimovahedi, S. Haghgoo, *Electrochim. Acta* **2007**, *53*, 1766–1774.
[31] M. Vidotti, S. I. Córdoba de Torresi, L. T. Kubota, *Sens. Actuators B* **2008**, *135*, 245–249.
[32] W. Huang, J. Zheng, Z. Li, *J. Phys. Chem. C* **2007**, *111*, 16902–16908.
[33] M. Jiang, R. Villagomez, A. Vo, L. G. Spears, *Electroanalysis* **2011**, *23*, 469–480.
[34] M. Hajjizadeh, A. Jabbari, H. Heli, A. A. Moosavi-Movahedi, A. Shafiee, K. Karimian, *Anal. Biochem.* **2008**, *373*, 337–348.
[35] J. Nai, J. Wu, L. Guo, S. Yang, *Cryst. Growth Des.* **2012**, *12*, 2653–2661.
[36] M. Fleischmann, K. Korinek, D. Pletcher, *J. Electroanal. Chem.* **1971**, *31*, 39–49.
[37] G. Horányi, *Electrochim. Acta* **1990**, *35*, 919–928.
[38] V. Dartois, J. Liu, J. A. Hoch, *Mol. Microbiol.* **1997**, *25*, 39–51.
[39] C. Kang, C. Qi, S. Feng, Z. Cai, *J. Mol. Struct.* **2002**, *579*, 235–245.
[40] C. Zhao, S. Shao, M. Li, K. Jiao, *Talanta* **2007**, *71*, 1769–1779.
[41] H. Kaiser, *Pure Appl. Chem.* **1973**, *34*, 35–61.
[42] C. Nan, J. Lu, C. Chen, Q. Peng, Y. Li, *J. Mater. Chem.* **2011**, *21*, 9994–9996.
[43] C. Delmas, C. Tessier, *J. Mater. Chem.* **1997**, *7*, 1439–1443.
[44] C. Tessier, P. H. Haumesser, P. Bernard, C. Delmas, *J. Electrochem. Soc.* **1999**, *146*, 2059–2067.
[45] R. S. Jayashree, P. V. Kamath, G. N. Subbanna, *J. Electrochem. Soc.* **2000**, *147*, 2029–2032.
[46] T. N. Ramesh, P. V. Kamath, C. Shivakumara, *J. Electrochem. Soc.* **2005**, *152*, A806–A810.
[47] M. Casas-Cabanas, J. Rodríguez-Carvajal, J. Canales-Vázquez, M. R. Palacín, *J. Mater. Chem.* **2006**, *16*, 2925–2939.
[48] B. C. Cornilsen, X. Shan, P. L. Loyselle, *J. Power Sources* **1990**, *29*, 453–466.
[49] B. C. Cornilsen, P. J. Karjala, P. L. Loyselle, *J. Power Sources* **1988**, *22*, 351–357.
[50] Y. G. Andreev, T. Lundstrom, *J. Appl. Crystallogr.* **1994**, *27*, 767–771.
[51] M. Rajamathi, P. V. Kamath, R. Seshadri, *J. Mater. Chem.* **2000**, *10*, 503–506.
[52] T. N. Ramesh, R. S. Jayashree, P. V. Kamath, *Clays Clay Miner.* **2003**, *51*, 570–576.
[53] A. S. Bookin, V. A. Drits, *Clays Clay Miner.* **1993**, *41*, 551–557.
[54] M. C. Bernard, R. Cortes, M. Keddam, H. Takenouti, P. Bernard, S. Senyarich, *J. Power Sources* **1996**, *63*, 247–254.
[55] M. J. Avena, M. V. Vazquez, R. E. Carbonio, C. P. De Pauli, V. A. Macagno, *J. Appl. Electrochem.* **1994**, *24*, 256–260.
[56] M. Casas-Cabanas, G. Binotto, D. Larcher, A. Lecup, V. Giordani, J.-M. Tarascon, *Chem. Mater.* **2009**, *21*, 1939–1947.
[57] X. Chen, L. Liu, P. Y. Yu, S. S. Mao, *Science* **2011**, *331*, 746–750.
[58] J. Pan, G. Liu, G. Q. Lu, H.-M. Cheng, *Angew. Chem.* **2011**, *123*, 2181–2185; *Angew. Chem. Int. Ed.* **2011**, *50*, 2133–2137.
[59] A. R. Verma, P. Krishna, *Polymorphism and Polytypism in Crystals*, Wiley, New York, **1996**, pp. 33.
[60] B. B. Prasad, D. Kumar, R. Madhuri, M. P. Tiwari, *Biosens. Bioelectron.* **2011**, *28*, 117–126.
[61] R.-M. Kong, X.-B. Zhang, Z. Chen, H.-M. Meng, Z.-L. Song, W. Tan, G.-L. Shen, R.-Q. Yu, *Anal. Chem.* **2011**, *83*, 7603–7607.
[62] A. Abbaspour, A. Ghaffarinejad, E. Safaei, *Talanta* **2004**, *64*, 1036–1040.

Received: August 24, 2012
Published online: December 18, 2012

